



Effect of anions on the anodic dissolution behavior of iron: An electrochemical and density functional theory study

Qin-Hao Zhang^{a,b,1}, Xian-Ze Meng^{b,1}, Xin-Ran Li^b, Hao Li^b, Lian-Kui Wu^b, Xin-Kun Suo^{a,*}, Fa-He Cao^{b,*}

^a Faculty of Mechanical Engineering and Mechanics, Ningbo University, Ningbo 315211, China

^b School of Materials, Sun Yat-Sen University, Shenzhen 518107, China



ARTICLE INFO

Keywords:

Iron
Kinetic parameters
Acid corrosion
Anodic dissolution
Electrochemical calculation

ABSTRACT

The influences of SO_4^{2-} , Cl^- , ClO_4^- and BF_4^- on the corrosion behavior of Fe in acidic solutions were quantitatively investigated through macro- and micro-electrochemical techniques, combined with DFT calculation. The electrochemical results showed that the corrosion rate increased in the order of BF_4^- , ClO_4^- , Cl^- and SO_4^{2-} , confirmed by the negative shift of OCP and E_{corr} , the decrease of R_{ct} and the increase of k_{eff}^0 of Fe oxidation. DFT calculation showed that the adsorption of SO_4^{2-} on Fe(100) surface was easier and stronger than Cl^- , and caused more significant Fe surface structure changes, resulting in more serious corrosion of Fe.

1. Introduction

Metals corrosion, a ubiquitous and costly behavior in various industries and infrastructure, is a complex and inevitable concern. Among the materials susceptible to corrosion, Fe and its alloys hold a prominent position. The deleterious effects of corrosion on Fe-based materials are manifold, encompassing structural damage, increased maintenance costs, and potential safety hazards in some cases [1]. The corrosion of Fe is intricately influenced by environmental factors, especially in marine, reinforced concrete and other heavily polluted environments, among which the presence of specific corrosive anions, such as Cl^- and SO_4^{2-} , plays a pivotal role [2,3]. Moreover, HBF_4 is commonly used as an electrolyte additive for Fe and other metal in electrolysis industry [4], and HClO_4 is often used as a supporting electrolyte in the research of corrosion inhibitors [5,6].

Over the years, extensive researches have been dedicated to understanding the intricate interplay between these corrosive anions and Fe corrosion [7–14]. It has been well-established that the Cl^- with small radius and strong penetration, can destroy the oxide film on the surface of Fe-based materials and significantly accelerate corrosion by involving in the Fe dissolution. This will result in the phenomenon commonly known as "pitting corrosion" due to its non-uniform surface adsorption [7–9]. Similarly, SO_4^{2-} can contribute to the corrosion of Fe in various environments, through the well-known consecutive dissolution

mechanism [10–12] and catalyzed mechanism [13,14]. The ClO_4^- and BF_4^- are considered to not strongly adsorb on metal surface nor have very strong tendencies to serve as ligands in complex formations [15,16].

At an early age, the polarization curve, combined with rotating ring-disk electrode technology, were mainly used to study the effect of anions on Fe corrosion [17–19], represented by Bockris [10–12] and Heusler [13,14]. However, it is an extremely difficult task to elucidate a complicated reaction mechanism only by the steady-state polarization curve, especially for the multi-electron transfer process of Fe anodic dissolution, because the mechanism determination is based on Tafel slope which involves many questionable and strongly restrictive assumptions [20]. Moreover, the polarization curve provides rather little information compared to the complexity of the process being investigated [21]. Electrochemical impedance spectroscopy (EIS) was later introduced to analyze the multistep processes of corrosion reaction, including the electron transfer, reaction intermediate and adsorbed phase [22–24]. However, it is somewhat suspicious to speculate the dissolution path via the number of capacitive or inductive loops, since the origin and physical meaning of capacitive or inductive loops are still difficult to interpret [25–27]. In addition, these macro-electrochemical techniques are difficult to quantitatively analyze the effect of anions on the Fe anodic dissolution, especially for the study of reaction intrinsic kinetics [28]. Therefore, multiple analytical methods, including macro-/micro-electrochemical techniques and theoretical calculation,

* Corresponding authors.

E-mail addresses: suoxinkun@nbu.edu.cn (X.-K. Suo), caofh5@mail.sysu.edu.cn (F.-H. Cao).

¹ Contributing equally to this work.

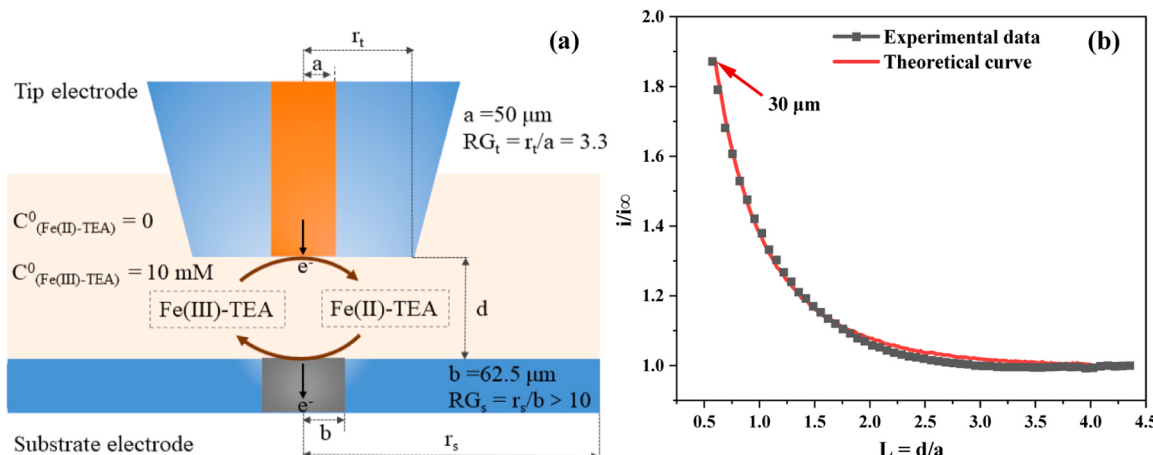


Fig. 1. (a) schematic representation for the reaction of Fe(III)/(II)-TEA redox mediator as the Fe tip approaching the Pt substrate. (b) SECM approach curve on Pt substrate ($E_s = -0.8$ V) with the Fe tip at $E_t = -1.15$ V.

needed to be combined to accurately analyze the corrosion reaction process.

The scanning probe techniques recently developed in the field of electrochemistry provide a new research method for the investigation on corrosion mechanism, including scanning vibrating electrode technique (SVET) [29–31], localized electrochemical impedance spectroscopy (LEIS) [32–34] and scanning electrochemical microscopy (SECM) [35–38]. Among them, SECM is a powerful technique due to its high spatial resolution and electrochemical sensitivity, to in situ characterize the morphology and redox activities of the metal/electrolyte interface [39,40]. Based on the multiple operation modes of SECM, it has been widely used in the research of dissolution [41], passivation [42] and localized corrosion [43,44] of Fe and its alloys in different anionic solutions. In our previous work [28], the modified tip generation/substrate collection (TG/SC) mode of SECM with Fe ultramicroelectrode (UME) as tip electrode has been utilized to instantaneously divide the apparent current of Fe corrosion process into Fe oxidation and proton reduction reaction, quantitatively obtaining the intrinsic kinetic parameters of hydrogen evolution and Fe oxidation reaction based on COMSOL simulation. However, most studies in the reported literatures focused on the dissolution mechanism and reactivity distribution of Fe surface, with little attention paid to the study of the effect of anions on the anodic dissolution of Fe, and a lack of atomic level elucidation of the anionic action mechanism.

Density functional theory (DFT) is a powerful tool for revealing the reaction mechanism through atomic vision and linking molecular modelling images with experimental results [45–48]. It has been widely used to evaluate the corrosion inhibition efficiency of inhibitors on Fe-based materials via modelling the adsorption of corrosion inhibitor on Fe surface [49,50]. In the aspect of simulating the interaction of corrosive mediums and Fe surface, Altarawneh et al., [51] conducted DFT simulation of Cl^- adsorption on Fe(100) surface to evaluate the effect of atomic chlorine on Fe anodic dissolution. Nong et al., [52] performed DFT simulation on the interaction between Cl^- and SO_4^{2-} on Fe(100) surface, and revealed that the mutual adsorption inhibition of these two anions on the Fe(100) surface was caused by their physical competitive adsorption, and their combined promotion of Fe corrosion was greater than that of a single anion.

In this work, the macro- and micro-electrochemical techniques, including OCP, polarization curve, EIS and SECM, combined with DFT calculation, were performed to comprehensively explore the influence of common anions, including SO_4^{2-} , Cl^- , ClO_4^- and BF_4^- , on the anodic dissolution of Fe in deaerated acidic solutions. The intrinsic kinetic parameters, including transfer coefficients α_{Fe} and standard rate constants k_{eff}^0 of Fe anodic dissolution in different anionic solutions were

quantitatively obtained by TG/SC mode of SECM. By establishing the simulation of Fe anodic dissolution behaviors with different anions through DFT calculation. Our efforts will help to better comprehend the effect of anions on the Fe anodic dissolution process.

2. Experimental section

2.1. Reagents and chemicals

Fluoroboric acid (HBF_4 , 40%), sodium fluoroborate (NaBF_4 , ≥98%), perchloric acid (HClO_4 , ≥99%), sodium perchlorate monohydrate ($\text{NaClO}_4 \cdot \text{H}_2\text{O}$, ≥99%), sulfuric acid (H_2SO_4 , 95.0–98.0%), sodium sulfate (Na_2SO_4 , ≥99%), hydrochloric acid (HCl , 36.0–38.0%), sodium chloride (NaCl , ≥99.5%), iron(III) sulfate hydrate ($\text{Fe}_2(\text{SO}_4)_3 \cdot x\text{H}_2\text{O}$), triethanolamine (TEA), sodium hydroxide (NaOH , ≥96.0%) were purchased from Sinopharm Chemical Reagent Co., Ltd. All chemical reagents were employed directly without further purification. The water used to prepare the electrolyte was purified by Milli-Q Direct Water Purification System ($\rho = 18 \text{ M}\Omega\text{-cm}$).

2.2. Instrumentation and measurement

The OCP, polarization curve and SECM measurements were performed on CHI920C bipotentiostat (CH Instruments, Inc., Shanghai, China) with radius 50 μm Fe UME as working electrode, Ag/AgCl (3 M KCl) as reference electrode and Pt wire as counter electrode. The SECM test also includes a 62.5 μm radius Pt substrate electrode for quantitative collection of species generated by Fe tip. The SECM experimental setup referred to our previous work [28,53]. EIS was performed on VersaSTAT 3F model potentiostat (Ametek Instruments, Inc., USA) with 1.5 mm radius pure Fe electrode as working electrode. Before EIS measurement, the Fe electrode was first reduced at -1.1 V in deaerated acidic solution for 5 min to remove the oxide film on surface [54]. Then a 30 min OCP test was performed to ensure that the electrode surface reaction reached a quasi-steady state. Finally, the EIS was measured at a 10 mV amplitude vs OCP in a frequency range from 10^5 Hz to 10^{-1} Hz. Unless otherwise specified, all potentials were relative to the potential of Ag/AgCl (3 M KCl).

The electrolyte for electrochemistry test was 5 mM HX + 0.1 M NaX solution with pH value around 2.3, where X was one of the SO_4^{2-} , Cl^- , ClO_4^- and BF_4^- . All the test solutions were deaerated for 15 min before measurements and the electrolytic cell was placed inside a sealed glovebag filled with high purity N_2 . All the tests were conducted at room temperature (25 °C).

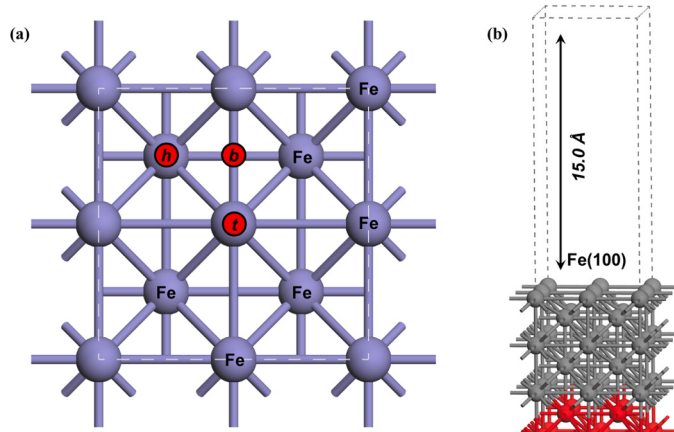


Fig. 2. The configuration of the optimized Fe(100) surface, (a) top view (b) side view.

2.3. Fe and Pt UME preparation

The Fe UME consists of Fe wire (radius 50 μm , 99.9% purity, Zhongnuo Advanced Material (Beijing) Technology Co., Ltd, China) and borosilicate capillary (OD: 1.0 mm; ID: 0.2 mm) manufactured with a laser puller (P-2000, Sutter Instruments Co., Novato, CA). Details for the preparation of Fe UME were given in our previous works [55,56]. The Fe UME was polished with sandpaper firstly, gradually increasing the mesh number from 400 to 1200, and then with 1 μm Al₂O₃ slurry until a smooth surface was obtained. A nickel wire was used to electrically contact with the Fe wire through conductive silver epoxy. Finally, the conduction of Fe UME was verified in 10 mM iron-triethanolamine (Fe(III)-TEA) solution with 2 M NaOH as supporting electrolyte.

The Pt UME was made by 62.5 μm radius Pt wire (Goodfellow, Huntingdon, UK), and borosilicate capillary (OD: 1.5 mm; ID: 0.86 mm, Sutter Instruments Co., Novato, CA) using a Vertical Micropipette Puller PC-10 (Narishige, Japan). The detailed preparation process could be carried out with reference to the procedure described elsewhere [57–59].

2.4. SECM tip-substrate gap control

The distance between Fe tip and Pt substrate was determined by the home-made Fe(III)-TEA, since its standard electrode potential ($E^0(\text{Fe}(\text{TEA})_2^{3+/2+}) = -0.82 \text{ V vs SHE}$ in 2 M NaOH solution [60]) was more negative than that of Fe ($E^0(\text{Fe}^{2+}/\text{Fe}) = -0.447 \text{ vs SHE}$) which did not undergo anodic dissolution of Fe during the tip approach. The synthesis of 10 mM Fe(III)-TEA + 2 M NaOH was described in detail in our previous publication [28].

Fig. 1a shows the schematic diagram of the two electrode reactions when the Fe tip approaches the Pt substrate using Fe(III)/II-TEA as the redox medium. The Fe tip held at -1.15 V where the reduction of Fe(III)-TEA was under diffusion control, and the Pt substrate was constant at -0.8 V to oxidize the generated Fe(II)-TEA based on the positive feedback mode of SECM. The approach curve were given in dimensionless form by plotting i_t/i_∞ (the Fe tip current i_t normalized by the current i_∞ measured in bulk solution) vs d/a (the distance d normalized by the radius a of Fe tip) was obtained, as shown in Fig. 1b. After fitting the experimental data with the theoretical simulation (the detailed simulation process could refer to our previous article [28]), the tip-substrate distance about 30 μm could be obtained.

2.5. Simulation method

The Fe(100) surface was selected to construct the simulation model, since it was a typical and widely used low-index face, and was

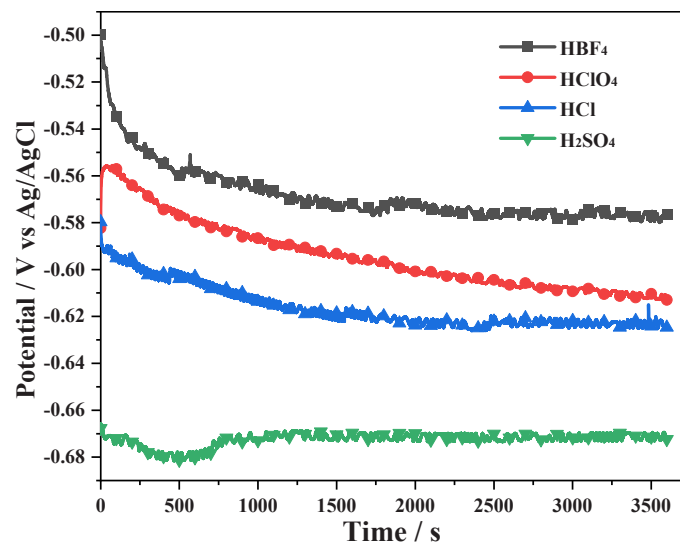


Fig. 3. Variation in OCP as a function of time for the Fe UME in deaerated acidic solution with different anions.

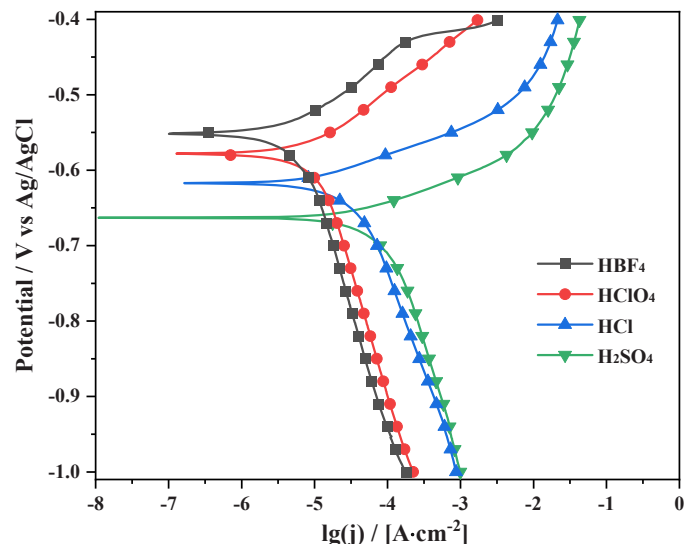


Fig. 4. Polarization curves of Fe electrode in deaerated acidic solution with different anions.

commonly used as a prototype substrate for investigating the interplay between adsorbate and Fe surface [61,62]. The pre-optimized lattice parameter of bulk Fe was 2.941 \AA in GGA-PBE functional, closing to the experimental results (2.866 \AA). As shown in Fig. 2, 7 layers unit cell structure was built by Fe-based substrate, and the Fe(100) surface was established. The two bottom layers of the Fe atoms were constrained, and the other layers were fully relaxed. The 2×2 periodic supercells with coverage of 0.25 ML were employed as the initial surfaces, to simulate the adsorption of different corrosive molecules (Fig. 2b). The vacuum layer of 15.0 \AA counteracted the longitudinal periodic interaction. The cutoff energy of plane wave was 340 eV, and the electron exchange interacted with ultrasoft pseudopotential. The k-points Monkhorst-Pack grid was chosen as $4 \times 4 \times 1$. The Tkatchenko-Scheffler method was chosen for dispersion correction. The convergence criteria of electronic self-consistent-field (SCF) tolerance was set to $10^{-5} \text{ eV}\cdot\text{atom}^{-1}$. All theoretical calculations were performed using spin-unrestricted plane-wave density functional theory (DFT) in the CASTEP module.

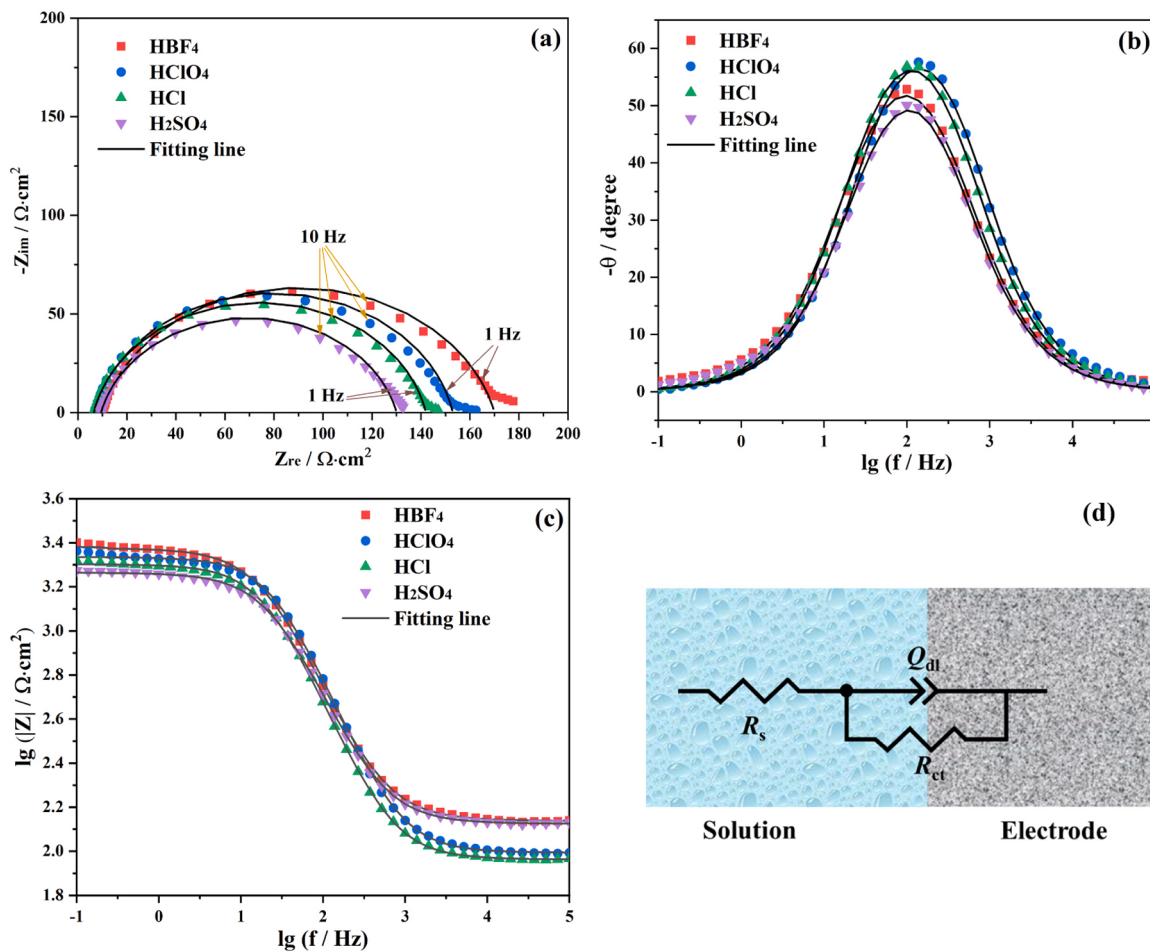


Fig. 5. Original EIS data and corresponding fitting results for Fe oxidation in deaerated acidic solution with different anions, (a) Nyquist plot (b) Bode-Angle frequency plot (c) Bode-Absolute frequency plot, and (d) the equivalent circuit model fitting the EIS experimental data.

3. Results and discussion

3.1. Macro-electrochemical measurement

The OCP provides information on the thermodynamic stability of sample surface in corrosive environment. The potential varies with time at different anions owing to the change of surface oxidation tendency [63]. Fig. 3 shows that the OCP shifted toward negative potentials in the BF₄⁻, ClO₄⁻ and Cl⁻ solutions with immersion time prolonged, while the OCP remained stable around -0.671 V in the SO₄²⁻ solution. Moreover, the OCP presented the most negative steady-state value in the SO₄²⁻ solution, followed by the Cl⁻, ClO₄⁻ and BF₄⁻ solution, demonstrating that the corrosion rate of Fe increased in the order of BF₄⁻ < ClO₄⁻ < Cl⁻ < SO₄²⁻.

The polarization curves of Fe electrode in the deaerated acidic solution with different anions are shown in Fig. 4. It was found that the corrosion potentials (\$E_{corr}\$) were gradually shifted toward a more negative direction in the order of BF₄⁻, ClO₄⁻, Cl⁻ and SO₄²⁻, while the corrosion current density (\$j_{corr}\$) gradually increased, indicating that the corrosion of Fe has the highest and slowest corrosion rate in SO₄²⁻ and BF₄⁻ solution, respectively. Note that the cathodic branches of the polarization curve in four different solutions had the same Tafel slope, indicating their similar corrosion behavior which the cathodic processes of proton reduction reaction and/or oxygen reduction reaction were all under charge transfer control. However, the slopes were different at the anode branches. The slopes at the anode branch for the Cl⁻ and SO₄²⁻ solutions were similar and the same as in BF₄⁻ and ClO₄⁻ solutions.

The Nyquist plot, Bode-Angle and Bode-Absolute frequency plots of

Fe electrode in different anionic solutions are shown in Fig. 5a-c. For the pure Fe electrode without passive film, the Nyquist plot showed a single capacitive loop which was related to the charge transfer of corrosion process (Fig. 5a). The shapes of the Nyquist plot did not change with the variation of anions, but the diameters of the capacitive loops increased with the following order of SO₄²⁻ < Cl⁻ < ClO₄⁻ < BF₄⁻, demonstrating the promoting effect on Fe oxidation in the order of SO₄²⁻ > Cl⁻ > ClO₄⁻ > BF₄⁻. In the Bode-Angle frequency plot, the impedance spectra were characterized by only one time constant (Fig. 5b). The magnitude plots showed that the module values increased with the order SO₄²⁻ < Cl⁻ < ClO₄⁻ < BF₄⁻. The results of Bode-Angle and Bode-Absolute frequency plots were in parallel with the Nyquist plot. This feature demonstrated that the oxidation rate of Fe increased. The EIS data were fitted by ZSimpWin software, and then the equivalent circuit (EC) and corresponding impedance parameters were obtained. Fig. 5a-c show that the fitted data agreed well with the experimental results. The EC was comprised of the solution resistance (\$R_s\$), the charge transfer resistance (\$R_{ct}\$) and the capacitive element of double layer (\$Q_{dl}\$), as shown in Fig. 5d. The \$Q_{dl}\$ and \$n\$ (dispersion coefficient) were used to replace the pure capacitance. Thus, the constant phase element (CPE) and capacitance (\$C_C\$) could be calculated via the following equations [64,65].

$$Z_{CPE} = \frac{1}{Y_0(j\omega)^n} \quad (1)$$

$$C_C = Y_0^{\frac{1}{n}} R_{ct}^{\frac{1-n}{n}} \quad (2)$$

Here, \$Y_0\$ represents the modulus, \$j\$ is the virtual root, \$\omega\$ means the

Table 1

Impedance parameters for Fe electrode in acidic solution with different anions.

Anions	R_s ($\Omega \text{ cm}^2$)	R_{ct} ($\Omega \text{ cm}^2$)	Q_{dl}	χ^2	
			Y_0 ($\Omega^{-1} \text{ cm}^{-2} \text{ s}^n$)	n	
BF_4^-	9.67	160.37	1.12×10^{-4}	0.85	6.36×10^{-4}
ClO_4^-	6.96	146.03	8.07×10^{-5}	0.88	6.14×10^{-4}
Cl^-	6.48	135.51	1.08×10^{-4}	0.88	2.74×10^{-4}
SO_4^{2-}	9.41	120.67	1.19×10^{-4}	0.86	3.94×10^{-4}

angular frequency, and n is the dimensionless index. The EIS parameters fitted are presented in Table 1. The goodness values (χ^2) in all solutions were on the order of 10^{-4} , indicating that the selected equivalent circuit was suitable and the obtained fitting parameters were accurate. The values of R_{ct} , which were attributed to the kinetic of the Fe anodic dissolution reaction [66], were observed to decrease with the order $\text{SO}_4^{2-} < \text{Cl}^- < \text{ClO}_4^- < \text{BF}_4^-$, indicating that the Fe showed a fastest corrosion rate in the SO_4^{2-} solution. These conclusions were consistent with the results of OCP and polarization curve.

After determining the tip-substrate distance, the cell was rinsed and the electrolyte was added. A linear sweep voltammetry (LSV)

experiment was initiated on Fe electrode at a scan rate of 5 mV/s from -1.1 V to -0.5 V , while the Pt substrate potential was set to 0.1 V for oxidizing the H_2 generated by tip electrode. Fig. 6a-d show the variation of Fe tip and Pt substrate current with tip potential under different anions. Since all these experiments were performed in deaerated acidic solution, the cathodic reduction current on Fe tip could only be attributed to the proton reduction current, and the corresponding Pt substrate current was the H_2 oxidation current. Therefore, the collection efficiency of the Pt substrate to the tip-generated H_2 could be determined by the ratio of substrate and tip current on the cathode polarization region. Due to the relatively close radius of the tip ($a = 50 \mu\text{m}$) and the substrate electrode ($a = 62.5 \mu\text{m}$), it was difficult for the Pt substrate to achieve 100% collection efficiency at $30 \mu\text{m}$ (the tip may hit the substrate when it was closer), but the proton reduction current at the tip could still be accurately obtained after correcting the substrate electrode for collection efficiency. In addition, the proton reduction current at the tip changed little at the same potential in different anionic solutions, which could be obviously seen from these figures at -1.1 V , indicating that the anions had little influence on the proton reduction current on Fe surface. Combined with the substrate current, the tip current started to be dominated by the oxidation of Fe when the Fe tip was swept higher than

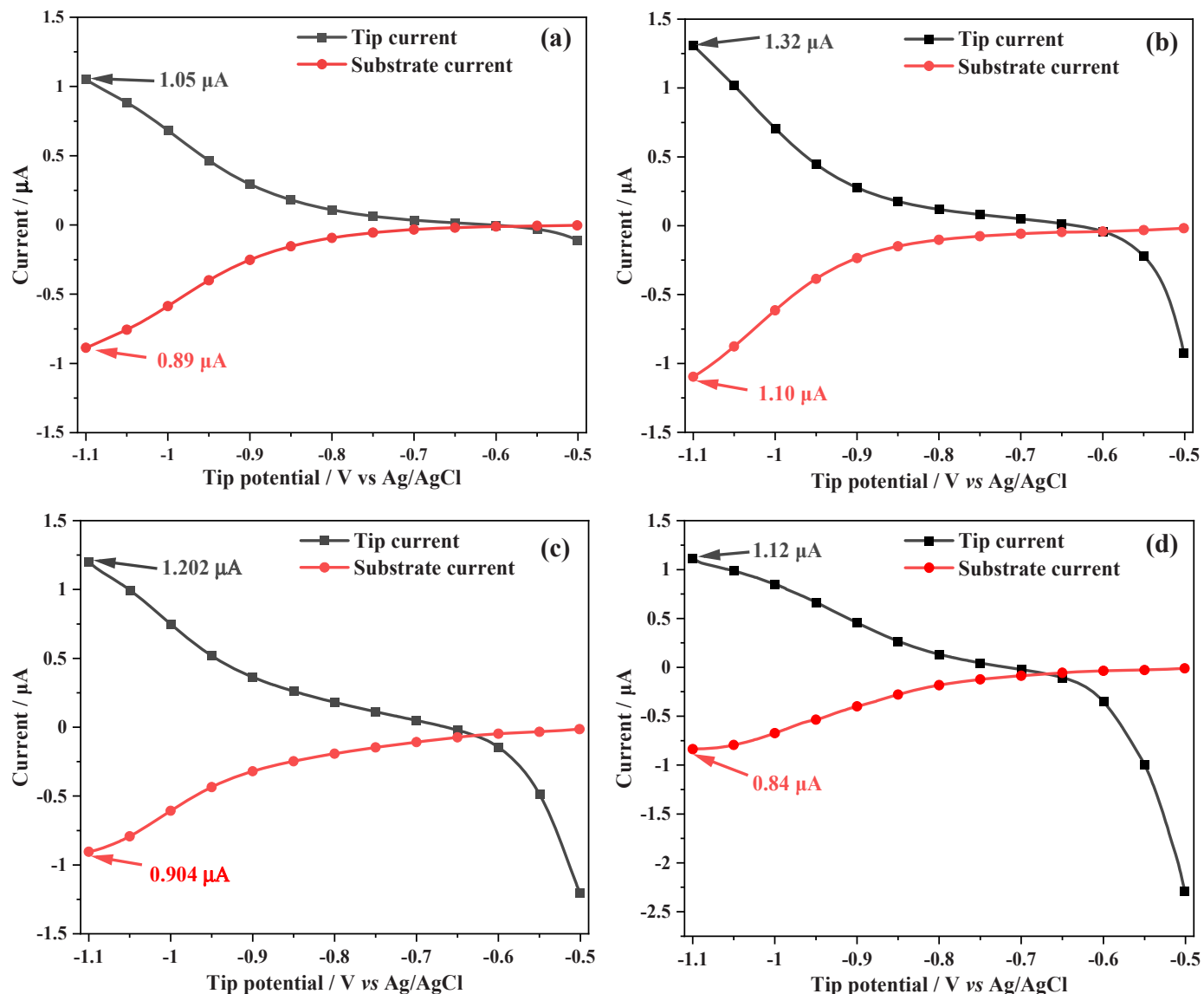


Fig. 6. LSV of Fe tip electrode on Pt substrate electrode in deaerated pH = 2.3 acidic solution with different anions, (a) $\text{HBF}_4^- + 0.1 \text{ M NaBF}_4$ (b) $\text{HClO}_4^- + 0.1 \text{ M NaClO}_4$ (c) $\text{HCl}^- + 0.1 \text{ M NaCl}$ (d) $\text{H}_2\text{SO}_4^- + 0.1 \text{ M Na}_2\text{SO}_4$ solution.

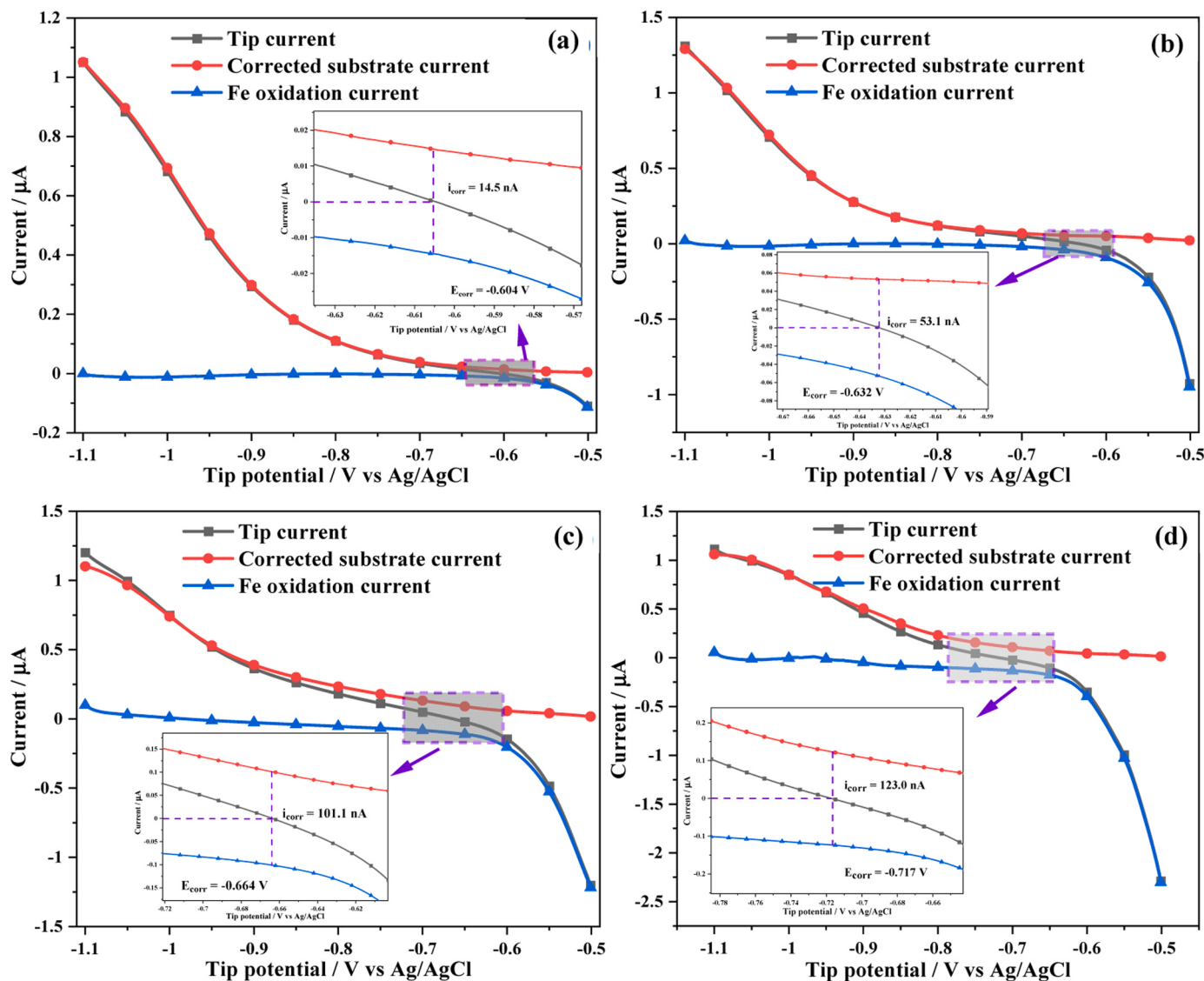


Fig. 7. After data processing of substrate current with collection efficiency in Fig. 6, the tip current, corrected substrate current and the difference between them as a function of tip potential in (a) $\text{HBF}_4 + 0.1 \text{ M NaBF}_4$ (b) $\text{HClO}_4 + 0.1 \text{ M NaClO}_4$ (c) $\text{HCl} + 0.1 \text{ M NaCl}$ (d) $\text{H}_2\text{SO}_4 + 0.1 \text{ M Na}_2\text{SO}_4$ solutions.

the potential where the tip current was 0.

Fig. 7 is the further data processing of Fig. 6 to obtain the variation of each reaction current with tip potential. The black line (■) in Fig. 7 represents the total tip current across the entire potential range. After correcting the reverse substrate current for collection efficiency, the red line (●) and blue line (▲) represent the proton reduction current at the Fe tip electrode and the difference between the tip current and proton reduction current (i.e. the Fe oxidation current), respectively. Fig. 7a-d show that the corrected substrate currents were well coincide with the tip current in cathodic polarization region, further illustrating that only proton reduction reactions occurred in this potential region. In addition, the corrected substrate currents tended to zero and the tip currents agreed well with the blue line (▲) in anodic polarization region,

indicating that the reaction occurring at the Fe tip was essentially the Fe oxidation process. Different from the slight difference of proton reduction current under different anionic solutions, the magnitude of Fe oxidation current significantly increased in the order of $\text{BF}_4^- < \text{ClO}_4^- < \text{Cl}^- < \text{SO}_4^{2-}$. For example, the Fe oxidation currents in the above four solutions were $-0.11 \mu\text{A}$, $-0.93 \mu\text{A}$, $-1.20 \mu\text{A}$ and $-2.29 \mu\text{A}$ at -0.30 V , respectively.

These insets in Fig. 7a-d were the enlarged view of the purple area to obtain the accurate corrosion current (i_{corr}) at the E_{corr} compared to the polarization curve. The E_{corr} , i_{corr} and corrosion current density (j_{corr} , the ratio of i_{corr} to electrode active area) in different anionic solutions were summarized in Table 2. It was found that the j_{corr} gradually increased, and the E_{corr} shifted negatively in the order of BF_4^- , ClO_4^- , Cl^- and SO_4^{2-} ,

Table 2

Kinetic parameters of Fe corrosion in different anionic acidic solutions.

Anions	Slope	Intercept	α_{Fe}	$k_{\text{eff}}^0 \text{ (cm/s)}$	$i_{corr} \text{ (nA)}$	$j_{corr} \text{ (mA/cm}^2)$	$E_{corr} \text{ (V)}$
BF_4^-	8.64	-4.07	0.74	4.43×10^{-7}	14.5	0.184	-0.604
ClO_4^-	8.78	-3.12	0.75	3.93×10^{-6}	53.1	0.676	-0.632
Cl^-	8.08	-2.914	0.76	6.3×10^{-6}	101.1	1.280	-0.664
SO_4^{2-}	7.17	-2.533	0.79	1.5×10^{-5}	123.0	1.570	-0.717

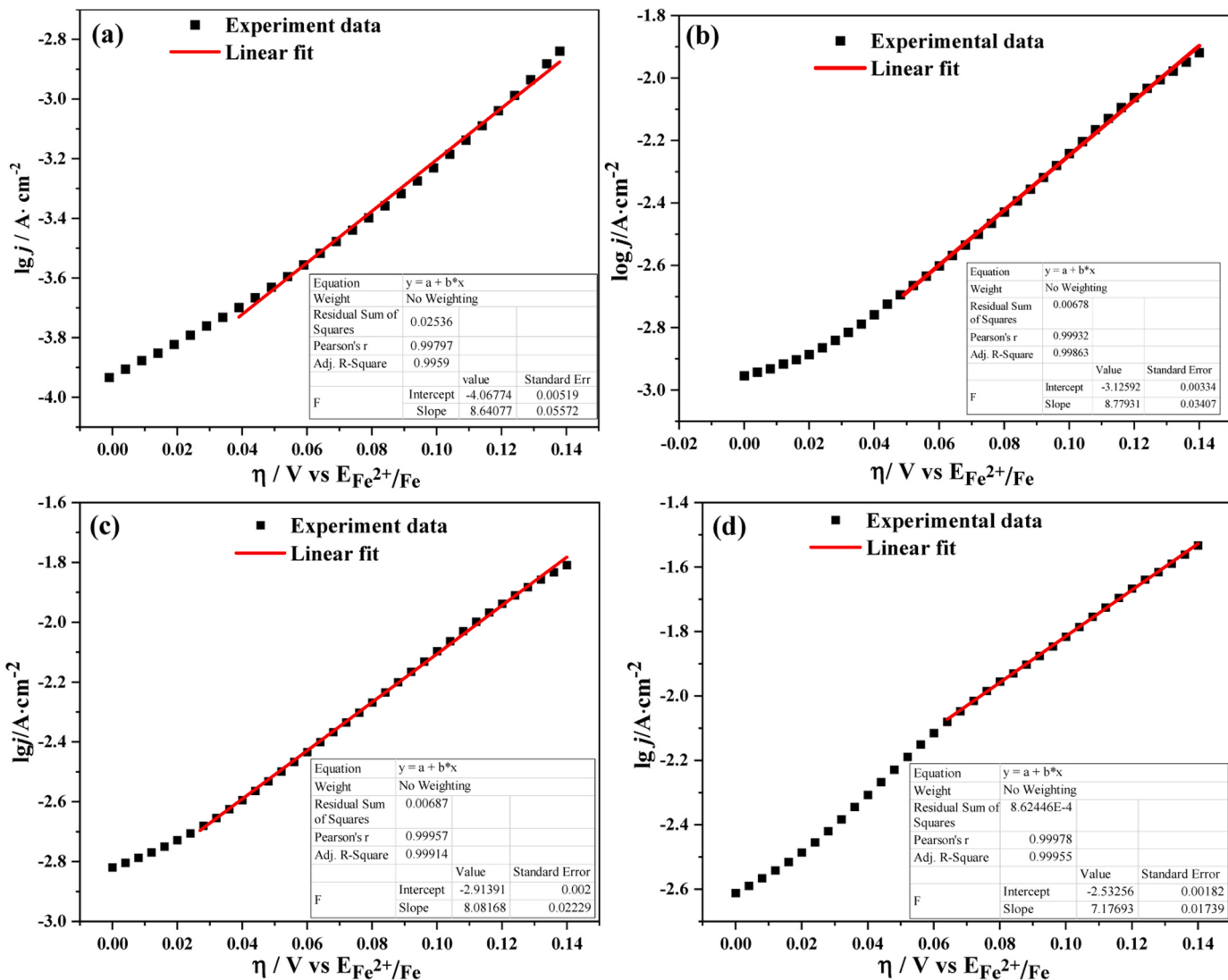


Fig. 8. The log j vs η (over potential) for Fe anodic oxidation branch and its linear fitting results in (a) $\text{HBF}_4 + 0.1 \text{ M NaBF}_4$, (b) $\text{HClO}_4 + 0.1 \text{ M NaClO}_4$, (c) $\text{HCl} + 0.1 \text{ M NaCl}$ and (d) $\text{H}_2\text{SO}_4 + 0.1 \text{ M Na}_2\text{SO}_4$ solutions.

indicating that the corrosion of Fe was most seriously in the SO_4^{2-} solution, followed by Cl^- and ClO_4^- solution, and the slowest in the BF_4^- solution.

Since the electrochemical reduction of Fe^{2+} could be ignored in the high anodic overpotential region, there was no feedback effect of Fe/Fe^{2+} and the kinetic parameters could be obtained by linearly fitting the Tafel region with the Equation [28,67]:

$$j = 2Fk_{\text{eff}}^0 c_{\text{Fe},0} \exp\left(\frac{2(1-\alpha_{\text{Fe}})F}{RT}\eta\right) \quad (3)$$

where j is the Fe oxidation current density, F is faradaic constant ($96,485 \text{ C mol}^{-1}$), k_{eff}^0 is the standard rate constant, $c_{\text{Fe},0}$ is Fe surface concentration (1 M for solid), α_{Fe} is transfer coefficient, T is room temperature (298 K), η is the over potential with respect to the standard electrode potential of Fe^{2+} (-0.44 V vs NHE). Converting the Eq. 3 into

$$\log j = \log\left(2Fk_{\text{eff}}^0 / 1000\right) + \frac{2 * (1 - \alpha_{\text{Fe}})F}{2.303 * RT} \eta \quad (4)$$

It could be seen from Eq. 4 that $\log j$ presented a linear relationship with η , thus the kinetic parameters of k_{eff}^0 and α_{Fe} could be obtained by the slope and intercept.

Fig. 8 shows the relationship between the $\log j$ of the Fe anode

dissolution branch and η , and its linear fitting results, where j is the ratio of Fe oxidation current obtained in Fig. 7 to the electrode active area exposed to solution. Fig. 8a-d show that the experimental data were highly consistent with the simulation results. The slope and intercept of linear fitting, as well as the calculated k_{eff}^0 and α_{Fe} , in different anionic solutions were listed in Table 2. As can be seen, α_{Fe} gradually increased in different anionic solutions in the order of $\text{BF}_4^- < \text{ClO}_4^- < \text{Cl}^- < \text{SO}_4^{2-}$, but the difference was small. Note that both the α_{Fe} were far away from 0.5 commonly used in corrosion studies, which could explain the large discrepancy between the theoretical Tafel slopes and experimental results. Regarding k_{eff}^0 , the difference from α_{Fe} was that k_{eff}^0 changed significantly in different anionic solutions with the same order of α_{Fe} . For example, the k_{eff}^0 was $1.5 \times 10^{-5} \text{ cm/s}$ in SO_4^{2-} solution, which was almost two orders of magnitude higher than that in BF_4^- solution ($4.43 \times 10^{-7} \text{ cm/s}$), indicating that Fe corroded faster than that in BF_4^- solution, and it was easier to reach equilibrium for the Fe^{2+}/Fe system in the SO_4^{2-} solution [68].

3.2. Corrosion morphology analysis

Fig. 9 shows the Fe surface morphology after immersion in different anionic solutions for 24 h. Fig. 9a₁₋₃ show that the surface of Fe were flat and without pitting after immersion in HBF_4 solution, indicating that it

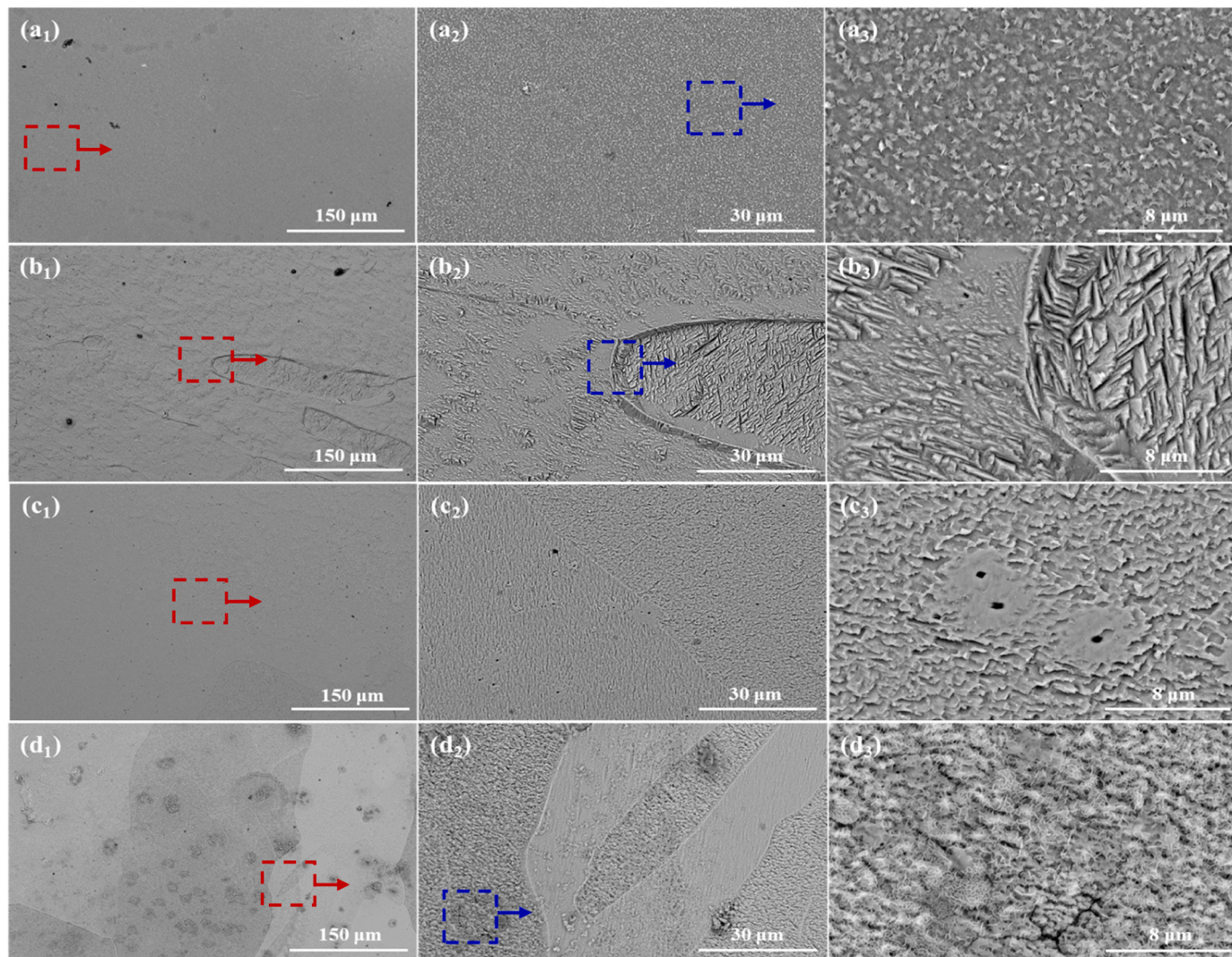


Fig. 9. The surface back scattered electron imaging of Fe electrode immersed in different anionic solutions for 24 h, where (a) 5 mM HBF_4 + 0.1 M NaBF_4 , (b) 5 mM HClO_4 + 0.1 M NaClO_4 , (c) 5 mM HCl + 0.1 M NaCl and (d) 5 mM H_2SO_4 + 0.1 M Na_2SO_4 solution. Figs. a_2-d_2 are the enlarged area of the red box in Figs. a_1-d_1 . Figs. a_3 , b_3 and d_3 are the enlarged area of the blue box in Figs. a_2 , b_2 and d_2 , respectively.

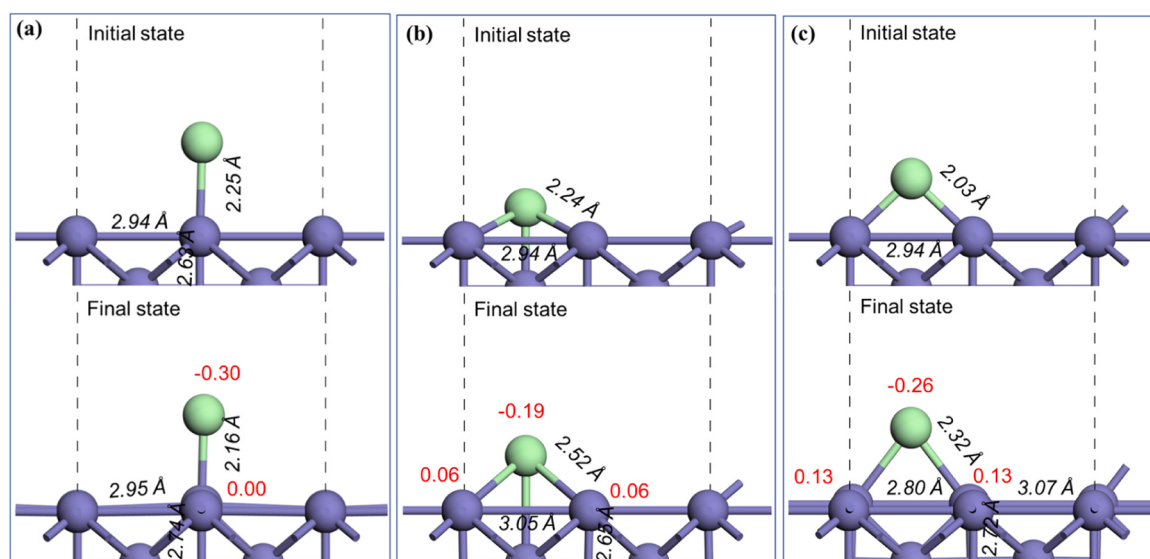


Fig. 10. The initial and final state of adsorption configurations for Cl^- on $\text{Fe}(100)$ surface, the (a) top, (b) hollow and (c) bridge site.

Table 3
The adsorption energy of Fe(100) surface adsorbed Cl^- and SO_4^{2-} .

Anions	Adsorption form	Adsorption energy (eV)
Cl ⁻	t	-3.6
	h	-3.8
	b	-3.9
SO ₄ ²⁻	2-O-down	-6.8
	3-O-down	-6.1
H ₂ O	t	-0.4

was carried out in a uniform corrosion form. However, the grains on the surfaces changed as Fe corroded in the HClO_4 solution (Fig. 9b₁₋₃), which may be caused by the difference in dissolution rate of different grain directions. Some of the grains corroded faster and the corrosion morphology showed a stepped shape. In the HCl solution (Fig. 9c₁₋₃), many pitting holes with diameters around 400 nm were observed in addition to grain boundaries. The surface morphology in H_2SO_4 solution was obviously different from that in the other three solutions, as shown in Fig. 9d₁₋₃. The Fe surface was covered by a large amount of corrosion products, which exhibited obvious flaky morphology [69].

3.3. DFT calculation

The DFT was only used here to calculate the adsorption behavior of Cl^- and SO_4^{2-} on Fe(100) surfaces, since the ClO_4^- and BF_4^- did not strongly adsorb on metal surfaces [15,16]. There were three adsorption sites for single atoms, namely top(t), hollow(h), and bridge(b) as shown in Fig. 2a. The adsorption energies of single Cl^- and SO_4^{2-} at different sites on the Fe(100) surface were calculated, respectively. Fig. 10 shows the adsorption configuration of Cl^- at three sites on Fe(100) surface, where the black number represents the key length, and the red number represents the Mulliken charge. The adsorption energies were listed in Table 3. The adsorption energies of Cl^- on top, hollow and bridge sites were -3.6 eV , -3.8 eV and -3.9 eV , which were significantly higher than the adsorption energy of water molecule (-0.4 eV), indicating that Cl^- was more easily adsorbed on Fe(100) surface than water molecule. Thus, the competitive adsorption effect of the water molecule could be ignored. Generally, the more negative adsorption energy means the stronger interaction between adsorbed species and metal surface [52]. Thus, the most stable configuration of Cl^- was b-type configuration (-3.9 eV). The effects of Cl^- on the surface structure of Fe(100) surface was also examined by calculating the changes in key length before and

after Cl^- adsorption. In the stable b-type configuration of Cl^- , the key length of the first layer changed from 2.94 Å at the initial state into 2.80 Å and 3.07 Å at the final state, while the distance between the first- and second-layer increased from 2.63 Å to 2.72 Å, implying that the adsorption of Cl^- caused the surface structure change of the Fe(100) surface.

The Mulliken charge was analyzed to further understand the adsorption and oxidation mechanism of Fe(100) surface after Cl^- adsorption. Fig. 10 shows that the Mulliken charges of Cl^- were -0.30 e (t), -0.19 e(h) and -0.26 e(b) , and the corresponding Mulliken charges of bonded Fe atoms were 0.00 e(t) , 0.06 e(h) , and 0.13 e(b) , respectively. This further proved that b-type configuration of Cl^- exhibited the strongest Mulliken charge polarity population and bonding stability. Moreover, the positive and negative values indicated that the Cl atom received electrons whereas Fe atom donated electrons. At the most Cl^- stable adsorption structure, the surface Fe atoms were most likely to provide electrons to Cl atoms, thus promoting the corrosion of Fe. The effect of ClO_4^- on promoting Fe corrosion was higher than that of BF_4^- , which may be due to the partial reduction of ClO_4^- under strong cathodic polarization to generate Cl^- [70,71].

Unlike Cl^- , SO_4^{2-} was composed of S and O atoms, so in simulating the adsorption of SO_4^{2-} on Fe(100) surface, the S or O atoms were located through different adsorption sites, and the result was shown in Fig. 11. It could be seen that SO_4^{2-} approached the Fe surface in three possible configurations: 1-O-down, 2-O-down and 3-O-down, and ultimately existed stably in two configurations: 2-O-down and 3-O-down. Among them, the adsorption energy of the 2-O-down configuration was the most negative (-6.8 eV), indicating the most stable form. At this form, the distance between the first- and second-layer increased from 2.63 Å to 2.75 Å, higher than the effect of Cl^- , indicating that the influence of SO_4^{2-} on the surface structure was higher than that of Cl^- , which was also consistent with previous report [52]. In addition, compared with the stable b-type configuration of Cl^- (-3.9 eV) shown in Fig. 10c, the adsorption energy of the most stable configuration of SO_4^{2-} was more negative than that of Cl^- adsorbed on Fe(100) surface, indicating that SO_4^{2-} was more easily adsorbed on Fe(100) surface than Cl^- . The Mulliken charge of S, O and Fe atoms on the Fe(100) surface after SO_4^{2-} adsorption showed that all the O atoms received electrons, and the Fe atoms were also found to donate electrons. However, the Mulliken charge of 3-O-down of SO_4^{2-} was much greater than Cl atom, indicating that the adsorption of SO_4^{2-} caused more electron loss of Fe surface as compared with the adsorption of Cl^- . The Mulliken charge of bonded Fe

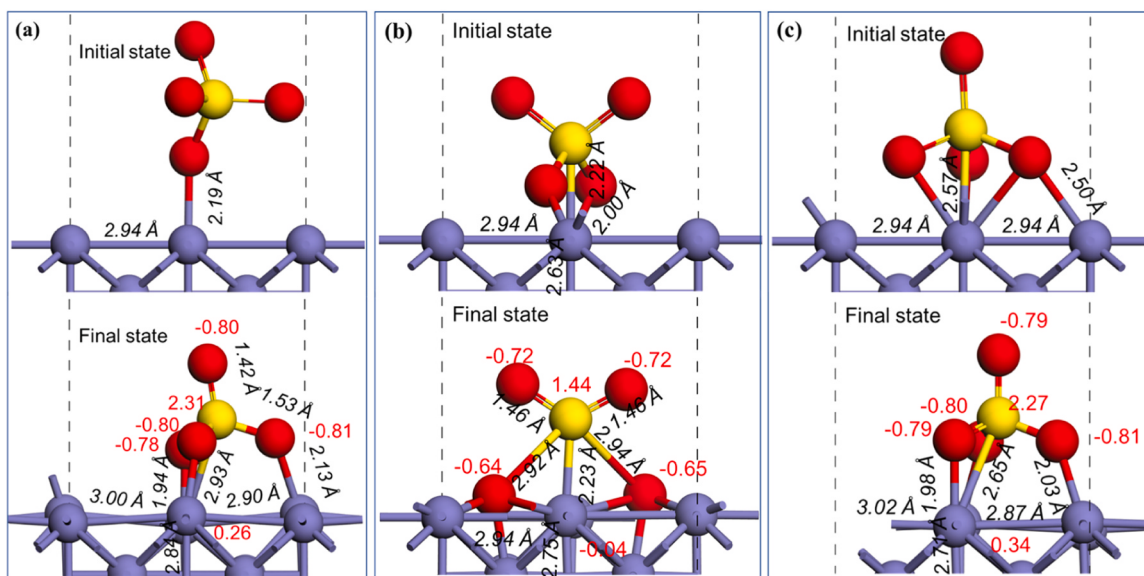


Fig. 11. The initial and final state of adsorption configurations for SO_4^{2-} on Fe(100) surface, the (a) 1-O-down, (b) 2-O-down and (c) 3-O-down.

with the 2-O-down configuration of SO_4^{2-} was -0.04 e, possibly due to the connection between Fe atoms and S atoms, resulting in a charge shift.

4. Conclusion

The influence of anions on the anodic dissolution of Fe in acidic solutions were studied through OCP, polarization curve, EIS and SECM, combining with DFT calculation. The results showed that Fe corroded most seriously in the SO_4^{2-} solution, followed by that in the Cl^- and ClO_4^- solution, and the slowest corrosion rate was found in the BF_4^- solution. The corresponding conclusions could be summarized as follows:

- (1) The corrosion of Fe in the SO_4^{2-} solution presented the most negative steady state OCP and E_{corr} , the highest j_{corr} , the lowest charge transfer resistance R_{ct} , followed by that in the Cl^- , ClO_4^- and BF_4^- solutions, indicating that Fe exhibited the highest corrosion rate in the SO_4^{2-} solution.
- (2) The intrinsic kinetic parameters of Fe corrosion, including transfer coefficient α_{Fe} and standard rate constant k_{eff}^0 , were obtained using the TG/SC mode of SECM, combined with COMSOL Multiphysics. The α_{Fe} under different anionic solutions differed little (0.76 ± 0.3), but were far different from 0.5 commonly used in corrosion research. However, the k_{eff}^0 significantly increased in the order of $\text{BF}_4^- < \text{ClO}_4^- < \text{Cl}^- < \text{SO}_4^{2-}$, indicating that the Fe corroded fastest in the SO_4^{2-} solution and it was easier to reach equilibrium for the Fe^{2+}/Fe system.
- (3) DFT calculation showed that the adsorption energy of SO_4^{2-} on Fe (100) surface was more negative than that of Cl^- , indicating that the adsorption of SO_4^{2-} was easier and stronger than that of Cl^- on Fe(100) surface, and caused more significant changes in the Fe surface structure. In addition, the Mulliken charge analysis showed that the adsorption of SO_4^{2-} caused more electron loss of Fe surface than Cl^- , demonstrating that the SO_4^{2-} caused more serious corrosion of Fe than Cl^- .

This work provides a multiple analytical method, including macro-/micro-electrochemical techniques and theoretical calculation for quantitatively investigating the influence of typical anions on Fe corrosion.

CRediT authorship contribution statement

Qin-Hao Zhang: Conceptualization, Methodology, Investigation, Writing - original draft, Funding acquisition. **Xian-Ze Meng:** Conceptualization, Investigation, DFT calculation, Writing review & editing, Funding acquisition. **Xin-Ran Li:** Formal analysis, Data curation. **Hao Li:** Validation, Writing review & editing. **Lian-Kui Wu:** Formal analysis, Writing-review & editing. **Xin-Kun Suo:** Resources, Conceptualization, Writing-review & editing. **Fa-He Cao:** Conceptualization, Project administration, Funding acquisition, Writing review & editing, Supervision..

Declaration of Competing Interest

The authors declare that they have no known competing financial interests or personal relationships that could have appeared to influence the work reported in this paper.

Data availability

Data will be made available on request.

Acknowledgements

We are very grateful to Professor Wei-Jin Chen (School of Materials, Sun Yat-sen University, China) for his guidance in DFT calculation. This

work was supported by the National Natural Science Foundation of China (Nos. 52201096, 52071347, 52201097 and 52371088); the National Materials Corrosion and Protection Data Center.

References

- [1] H. Lotz, D. Neff, F. Mercier-Bion, C. Bataillon, P. Dillmann, E. Gardés, I. Monnet, J. J. Dynes, E. Foy, Localised corrosion of iron and steel in the Callovo-Oxfordian porewater after 3 months at 120 °C: Characterizations at micro and nanoscale and formation mechanisms, *Corros. Sci.* 219 (2023) 111235.
- [2] Z. Fu, X. Zhang, X. Guo, D. Legut, D. Zhang, Understanding atomic interaction between cuprous oxide film and aggressive chloride solution, *Corros. Sci.* 227 (2024) 111718.
- [3] Z. Shao, D. Yu, D. Shao, Y. Du, D. Zheng, Z. Qiu, B. Wu, A protective role of Cl^- ion in corrosion of stainless steel, *Corros. Sci.* 226 (2024) 111631.
- [4] Z. Razaghi, M. Rezaei, S.H. Tabaian, Electrochemical noise and impedance study on the corrosion of electroplated Ni-Cr coatings in HBF_4 aqueous solution, *J. Electroanal. Chem.* 859 (2020) 113838.
- [5] H. Ma, G. Li, S. Chen, S. Zhao, X. Cheng, Impedance investigation of the anodic iron dissolution in perchloric acid solution, *Corros. Sci.* 44 (2002) 1177–1191.
- [6] D.K. Kozlica, B. Hernández-Concepción, J. Izquierdo, R.M. Souto, I. Milošev, In situ, real-time imaging of redox-active species on Al/Cu galvanic couple and corrosion inhibition with 2-mercaptopbenzimidazole and octylphosphonic acid, *Corros. Sci.* 217 (2023) 111114.
- [7] B. Zhang, J. Wang, B. Wu, X.W. Guo, Y.J. Wang, D. Chen, Y.C. Zhang, K. Du, E. E. Oguzie, X.L. Ma, Unmasking chloride attack on the passive film of metals, *Nat. Commun.* 9 (2018) 2559.
- [8] P. Li, M. Du, Effect of chloride ion content on pitting corrosion of dispersion-strengthened-high-strength steel, *Corros. Commun.* 7 (2022) 23–34.
- [9] Z. Liu, L.M. Zhang, W.Q. Chen, A.L. Ma, Y. Zheng, W. Yan, Y.F. Li, Y.Y. Shan, X. W. Hu, C. Kan, Y.G. Zheng, Effect of chloride ion on the corrosion behavior of SiN stainless steel in concentrated hot nitric acid media, *Corros. Sci.* 225 (2023) 111604.
- [10] J.O.M. Bockris, D. Drazic, A.R. Despic, The electrode kinetics of the deposition and dissolution of iron, *Electrochim. Acta* 4 (1961) 325–361.
- [11] J.O.M. Bockris, D. Drazic, The kinetics of deposition and dissolution of iron: effect of alloying impurities, *Electrochim. Acta* 7 (1962) 293–313.
- [12] E.J. Kelly, The active iron electrode: I. Iron dissolution and hydrogen evolution reactions in acidic sulfate solutions, *J. Electrochem. Soc.* 112 (1965) 124–131.
- [13] K.E. Heusler, G.H. Cartledge, The influence of iodide ions and carbon monoxide on the anodic dissolution of active iron, *J. Electrochem. Soc.* 108 (1961) 732–740.
- [14] K.F. Bonhoeffer, K.E. Heusler, Abhängigkeit der anodischen Eisenauflösung von der Säurekonzentration, *Z. Phys. Chem.* 8 (1956) 390–393.
- [15] R.J. Chin, K. Nobe, Electrodissolution kinetics of iron in chloride solutions: III. Acidic solutions, *J. Electrochem. Soc.* 119 (1972) 1457–1461.
- [16] K.C. Leonard, A.J. Bard, The study of multireactional electrochemical interfaces via a tip generation/substrate collection mode of scanning electrochemical microscopy: the hydrogen evolution reaction for Mn in acidic solution, *J. Am. Chem. Soc.* 135 (2013) 15890–15896.
- [17] W.J. Lorenz, G. Eichhorn, C. Mayer, Über den Einfluß von sulfationen auf die kinetik der anodischen Eisenauflösung in sauren lösungen, *Corros. Sci.* 7 (1967) 357–365.
- [18] W.J. Lorenz, Der einfluss von halogenidionen auf die anodische auflösung des eisens, *Corros. Sci.* 5 (1965) 121–131.
- [19] D.M. Brasher, Role of the anion in relation to metallic corrosion and inhibition, *Nature* 193 (1962) 868–869.
- [20] E. McCafferty, Validation of corrosion rates measured by the Tafel extrapolation method, *Corros. Sci.* 47 (2005) 3202–3215.
- [21] M. Keddam, O.R. Mattos, H. Takenouti, Reaction model for iron dissolution studied by electrode impedance: I. Experimental results and reaction model, *J. Electrochem. Soc.* 128 (1981) 257–266.
- [22] C. Gabrielli, M. Keddam, Contribution of electrochemical impedance spectroscopy to the investigation of the electrochemical kinetics, *Electrochim. Acta* 41 (1996) 957–965.
- [23] D.A. Harrington, Electrochemical impedance of multistep mechanisms: a general theory, *J. Electroanal. Chem.* 449 (1998) 9–28.
- [24] C.-M. Deng, D.-H. Xia, R. Zhang, Y. Behnamian, W. Hu, N. Birbilis, On the localized corrosion of AA5083 in a simulated dynamic seawater/air interface—Part 2: effects of wetting time, *Corros. Sci.* 221 (2023) 111367.
- [25] M. Keddam, O.R. Mattos, H. Takenouti, Reaction model for iron dissolution studied by electrode impedance: II. Determination of the reaction model, *J. Electrochem. Soc.* 128 (1981) 266–274.
- [26] O.E. Barcia, O.R. Mattos, The role of chloride and sulphate anions in the iron dissolution mechanism studied by impedance measurements, *Electrochim. Acta* 35 (1990) 1003–1009.
- [27] O.E. Barcia, O.R. Mattos, Reaction model simulating the role of sulphate and chloride in anodic dissolution of iron, *Electrochim. Acta* 35 (1990) 1601–1608.
- [28] Q.H. Zhang, Z.N. Ye, Z.J. Zhu, X.Y. Liu, J.Q. Zhang, F.H. Cao, Separation and kinetic study of iron corrosion in acidic solution via a modified tip generation/substrate collection mode by SECM, *Corros. Sci.* 139 (2018) 403–409.
- [29] H. Li, Q.-H. Zhang, X.-Z. Meng, P. Liu, L.-K. Wu, F.-H. Cao, A novel cerium organic network modified graphene oxide prepared multifunctional waterborne epoxy-based coating with excellent mechanical and passive/active anti-corrosion properties, *Chem. Eng. J.* 465 (2023) 142997.

- [30] A. Cristoforetti, J. Izquierdo, R.M. Souto, F. Deflorian, M. Fedel, S. Rossi, In-situ measurement of electrochemical activity related to filiform corrosion in organic coated steel by scanning vibrating electrode technique and scanning micropotentiometry, *Corros. Sci.* 227 (2024) 111669.
- [31] H. Li, Q.-H. Zhang, X.-Z. Meng, H.-J. Yan, H.-S. Hu, L.-K. Wu, F.-H. Cao, Active/passive protection and anti-UV waterborne epoxy coatings based on low defect functionalized PDA-GO-CeO₂ material for excellent corrosion control, *Chem. Eng. J.* 479 (2024) 147859.
- [32] L.M. Calado, M.G. Taryba, Y. Morozov, M.J. Carmezim, M.F. Montemor, Novel smart and self-healing cerium phosphate-based corrosion inhibitor for AZ31 magnesium alloy, *Corros. Sci.* 170 (2020) 108648.
- [33] H. Li, Y. Qiang, W. Zhao, S. Zhang, 2-Mercaptobenzimidazole-inbuilt metal-organic-frameworks modified graphene oxide towards intelligent and excellent anti-corrosion coating, *Corros. Sci.* 191 (2021) 109715.
- [34] M. Attai, M.G. Taryba, R.A. Shakoob, R. Kahraman, A.C. Marques, M. F. Montemor, Highly protective polyolefin coating modified with ceria nano particles treated with N,N,N',N'-Tetrakis(2-hydroxyethyl)ethylenediamine for corrosion protection of carbon steel, *Corros. Sci.* 198 (2022) 110162.
- [35] D.-H. Xia, J. Wang, Z. Wu, Z. Qin, L. Xu, W. Hu, Y. Behnamian, J.-L. Luo, Sensing corrosion within an artificial defect in organic coating using SECM, *Sens. Actuators B-Chem.* 280 (2019) 235–242.
- [36] L. Huang, W. Chang, D. Zhang, Y. Huang, Z. Li, Y. Lou, H. Qian, C. Jiang, X. Li, A. Mol, Acceleration of corrosion of 304 stainless steel by outward extracellular electron transfer of *Pseudomonas aeruginosa* biofilm, *Corros. Sci.* 199 (2022) 110159.
- [37] H.C. Qian, W.W. Chang, T.Y. Cui, Z. Li, D.W. Guo, C.T. Kwok, L.M. Tam, D. W. Zhang, Multi-mode scanning electrochemical microscopic study of microbiologically influenced corrosion mechanism of 304 stainless steel by thermoacidophilic archaea, *Corros. Sci.* 191 (2021) 109751.
- [38] H. Qian, D. Zhang, T. Cui, W. Chang, F. Cao, C. Du, X. Li, Accelerating effect of catalase on microbiologically influenced corrosion of 304 stainless steel by the halophilic archaeon *Natronorubrum tibetense*, *Corros. Sci.* 178 (2021) 109057.
- [39] X.R. Li, X.Z. Meng, Q.H. Zhang, H.R. Cai, Z.Z. Yan, L.K. Wu, F.H. Cao, In situ studies of hydrogen evolution kinetics on pure titanium surface: the effects of pre-reduction and dissolved oxygen, *J. Phys. Chem. C* 126 (2022) 1828–1844.
- [40] X.R. Li, Q.H. Zhang, X.Z. Meng, L.K. Wu, F.H. Cao, Effect of pretreatments on the hydrogen evolution kinetics of pure titanium using impedance and SECM technologies, *Corros. Sci.* 191 (2021) 109726.
- [41] K. Fushimi, M. Seo, An SECM observation of dissolution distribution of ferrous or ferric ion from a polycrystalline iron electrode, *Electrochim. Acta* 47 (2001) 121–127.
- [42] J. Izquierdo, L. Martín-Ruiz, B.M. Fernández-Pérez, L. Fernández-Mérida, J. Santana, R.M. Souto, Imaging local surface reactivity on stainless steels 304 and 316 in acid chloride solution using scanning electrochemical microscopy and the scanning vibrating electrode technique, *Electrochim. Acta* 134 (2014) 167–175.
- [43] Z.J. Zhu, Q.H. Zhang, P. Liu, J.Q. Zhang, F.H. Cao, Quasi-simultaneous electrochemical/chemical imaging of local Fe²⁺ and pH distributions on 316 L stainless steel surface, *J. Electroanal. Chem.* 871 (2020) 114107–114115.
- [44] Z.N. Ye, Z.J. Zhu, Q.H. Zhang, X.Y. Liu, J.Q. Zhang, F.H. Cao, In situ SECM mapping of pitting corrosion in stainless steel using submicron Pt ultramicroelectrode and quantitative spatial resolution analysis, *Corros. Sci.* 143 (2018) 221–228.
- [45] H. Li, S. Zhang, Y. Qiang, Corrosion retardation effect of a green cauliflower extract on copper in H₂SO₄ solution: Electrochemical and theoretical explorations, *J. Mol. Liq.* 321 (2021) 114450.
- [46] X.Z. Meng, X.R. Li, Q.H. Zhang, L.K. Wu, F.H. Cao, Temperature-dependent structure of 3.5 wt % NaCl aqueous solution: theoretical and Raman investigation, *J. Mol. Struct.* 1253 (2022) 132279.
- [47] X.R. Li, X.Z. Meng, Q.H. Zhang, L.K. Wu, Q.Q. Sun, H.Q. Deng, S.J. Sun, F.H. Cao, Insight into oxygen reduction activity and pathway on pure titanium using scanning electrochemical microscopy and theoretical calculations, *J. Colloid Interface Sci.* 643 (2023) 551–562.
- [48] Y. Ji, Q. Hu, D.-H. Xia, J.-L. Luo, Corrosion susceptibility of passive films on 1060, 2024, and 5083 aluminum alloys: experimental study and first-principles calculations, *J. Electrochem. Soc.* 170 (2023) 041505.
- [49] G.L.F. Mendonça, S.N. Costa, V.N. Freire, P.N.S. Casciano, A.N. Correia, Pd Lima-Neto, Understanding the corrosion inhibition of carbon steel and copper in sulphuric acid medium by amino acids using electrochemical techniques allied to molecular modelling methods, *Corros. Sci.* 115 (2017) 41–55.
- [50] Z. Zhang, N. Tian, W. Zhang, X. Huang, L. Ruan, L. Wu, Inhibition of carbon steel corrosion in phase-change-materials solution by methionine and proline, *Corros. Sci.* 111 (2016) 675–689.
- [51] M. Altarawneh, S.A. Saraireh, Theoretical insight into chlorine adsorption on the Fe(100) surface, *Phys. Chem. Chem. Phys.* 16 (2014) 8575–8581.
- [52] Z. Chen, Z. Wei, Y. Chen, Y. Nong, C. Yi, Molecular insight into iron corrosion induced by chloride and sulphate, *Comput. Mater. Sci.* 209 (2022) 111429.
- [53] Q.H. Zhang, P. Liu, Z.J. Zhu, Z.N. Ye, J.Q. Zhang, F.H. Cao, X.G. Li, Quantitative analysis of the polarization behavior of iron in an aerated acidic solution using SECM, *Electrochim. Commun.* 93 (2018) 143–147.
- [54] T. Tsuru, E.-i Fujii, S. Haruyama, Passivation of iron and its cathodic reduction studied with a rotating ring-disk electrode, *Corros. Sci.* 31 (1990) 655–660.
- [55] J. Kim, B.-K. Kim, S.K. Cho, A.J. Bard, Tunneling ultramicroelectrode: nanoelectrodes and nanoparticle collisions, *J. Am. Chem. Soc.* 136 (2014) 8173–8176.
- [56] B.-K. Kim, J. Kim, A.J. Bard, Electrochemistry of a single attoliter emulsion droplet in collisions, *J. Am. Chem. Soc.* 137 (2015) 2343–2349.
- [57] F. Cao, J. Kim, A.J. Bard, Detection of the short-lived cation radical intermediate in the electrochemical oxidation of N,N-Dimethylaniline by scanning electrochemical microscopy, *J. Am. Chem. Soc.* 136 (2014) 18163–18169.
- [58] J. Kim, J.E. Dick, A.J. Bard, Advanced electrochemistry of individual metal clusters electrodeposited atom by atom to nanometer by nanometer, *Acc. Chem. Res.* 49 (2016) 2587–2595.
- [59] S.J. Percival, J.E. Dick, A.J. Bard, Cathodically dissolved platinum resulting from the O₂ and H₂O₂ reduction reactions on platinum ultramicroelectrodes, *Anal. Chem.* 89 (2017) 3087–3092.
- [60] A.J. Bard, M.V. Mirkin, Scanning Electrochemical Microscopy, 2nd ed., Marcel Dekker, New York, 2012.
- [61] Z. Chen, Y. Nong, Y. Chen, J. Chen, B. Yu, Study on the adsorption of OH⁻ and CaOH⁺ on Fe(100) surface and their effect on passivation of steel bar: experiments and DFT modelling, *Corros. Sci.* 174 (2020) 108804.
- [62] J. Zhu, G. Zhou, F. Niu, Y. Shi, Z. Du, G. Lu, Z. Liu, Understanding the inhibition performance of novel dibenzimidazole derivatives on Fe(110) surface: DFT and MD simulation insights, *J. Mater. Res. Technol.* 17 (2022) 211–222.
- [63] S. Choudhary, A. Garg, K. Mondal, Relation between open circuit potential and polarization resistance with rust and corrosion monitoring of mild steel, *J. Mater. Eng. Perform.* 25 (2016) 2969–2976.
- [64] G.J. Brug, A.L.G. van den Eeden, M. Sluyters-Rehbach, J.H. Sluyters, The analysis of electrode impedances complicated by the presence of a constant phase element, *J. Electroanal. Chem. Interfacial Electrochem.* 176 (1984) 275–295.
- [65] P. Liu, Q.H. Zhang, J.Q. Zhang, J.M. Hu, F.H. Cao, Rapid synthesis of highly oriented hydrophobic silicalite-1 zeolite films on alloy steel at lower temperature for corrosion protection, *Chem. Eng. J.* 430 (2022) 133173.
- [66] R. De Motte, E. Basilico, R. Mingant, J. Kittel, F. Ropital, P. Combrade, S. Necib, V. Deydier, D. Crusset, S. Marcellin, A study by electrochemical impedance spectroscopy and surface analysis of corrosion product layers formed during CO₂ corrosion of low alloy steel, *Corros. Sci.* 172 (2020) 108666.
- [67] Q.H. Zhang, Z.J. Zhu, P. Liu, J.Q. Zhang, F.H. Cao, Corrosion electrochemical kinetic study of copper in acidic solution using scanning electrochemical microscopy, *J. Electrochim. Soc.* 166 (2019) C401–C409.
- [68] A.J. Bard, L.R. Faulkner, J. Leddy, C.G. Zoski, *Electrochemical Methods: Fundamentals and Applications*, 2nd ed., Wiley, New York, 1980.
- [69] P. Liu, L.L. Hu, Z.X. Yang, Z.S. Yu, J.M. Hu, Y.Q. Chen, F.F. Wu, F.H. Cao, Investigation of microstructure and corrosion behavior of weathering steel in aqueous solution containing different anions for simulating service environments, *Corros. Sci.* 170 (2020) 108686.
- [70] M.A. Amin, Metastable and stable pitting events on Al induced by chlorate and perchlorate anions—Polarization, XPS and SEM studies, *Electrochim. Acta* 54 (2009) 1857–1863.
- [71] L. Xing, O. Borodin, G.D. Smith, W. Li, Density functional theory study of the role of anions on the oxidative decomposition reaction of propylene carbonate, *J. Phys. Chem. A* 115 (2011) 13896–13905.